Estimating melt onset over Arctic sea ice from time series multi-sensor Sentinel-1 and RADARSAT-2 backscatter

Howell, Stephen E L ; Small, David ; Rohner, Christoph ; Mahmud, Mallik S ; Yackel, John J ; Brady, Michael

Abstract: Information on the timing of melt onset over sea ice is important for understanding the Arctic's changing climate. The daily temporal resolution of passive microwave brightness temperatures provides the most widely utilized observations to detect melt onset but are limited to a spatial resolution of 25 km. Wide-swath synthetic aperture radar (SAR) imagery provides a much higher spatial resolution (20–100 m) but melt onset detection remains challenging because of i) insufficient temporal resolution to facilitate accurate melt onset detection, ii) inconsistent viewing geometries and iii) limited image availability across the Arctic. Here, we construct high temporal resolution composite gamma nought backscatter products (1 day, 1–2 day and 2–4 day) using Sentinel-1 and RADARSAT-2 over a close-to-seamless revisit region located in northern Canadian Arctic and Greenland for estimating melt onset over Arctic sea ice in 2016 and 2017. We employ the necessary radiometric terrain flattening and local resolution weighting techniques to generate normalised backscatter over the entire study region, removing restrictions limiting analysis to a single sensor or track's swath width by integrating both ascending and descending passes into the composite products. Results indicate that higher temporal resolution multi-sensor composite gamma nought products (1 day) that make use of the most imagery provide a robust temporal evolution of the backscatter. This allows for more representative estimates of melt onset as it is easier to separate the melt onset threshold from winter variability that is otherwise a considerable challenge for SAR based melt onset algorithms because of inconsistent temporal resolution. Multi-sensor composite gamma naught melt onset detection is in good agreement with melt onset estimates derived from the Advance Scatterometer (ASCAT) backscatter values and passive microwave brightness temperatures over homogenous sea ice regions but very noticeable improvement was found within narrow channels and regions with more heterogeneous sea ice. In anticipation of the availability of data from even more SAR satellites with the launch of the RADARSAT Constellation Mission, the multi-sensor composite gamma nought approach presented here may offer the most robust approach to estimate the timing of melt onset over sea ice across the Arctic using high spatiotemporal resolution SAR.

DOI: https://doi.org/10.1016/j.rse.2019.04.031

Originally published at:
Howell, Stephen E L; Small, David; Rohner, Christoph; Mahmud, Mallik S; Yackel, John J; Brady, Michael (2019). Estimating melt onset over Arctic sea ice from time series multi-sensor Sentinel-1 and RADARSAT-2 backscatter. Remote Sensing of Environment, 229:48-59.
DOI: https://doi.org/10.1016/j.rse.2019.04.031

Remote Sensing of Environment 229 (2019) 48–59

Contents lists available at ScienceDirect

Remote Sensing of Environment

journal homepage: www.elsevier.com/locate/rse

Estimating melt onset over Arctic sea ice from time series multi-sensor Sentinel-1 and RADARSAT-2 backscatter

Stephen E.L. Howell[a,*], David Small[b], Christoph Rohner[b], Mallik S. Mahmud[c], John J. Yackel[c], Michael Brady[a]

[a] Climate Research Division, Environment and Climate Change Canada, Toronto, Ontario, Canada
[b] UZH-RSL - Remote Sensing Laboratories, University of Zürich, Zürich, Switzerland
[c] Department of Geography, University of Calgary, Calgary, Alberta, Canada

ARTICLE INFO

Keywords:
Sea ice
Melt onset
SAR
Gamma naught
Sentinel-1
RADARSAT-2

ABSTRACT

Information on the timing of melt onset over sea ice is important for understanding the Arctic's changing climate. The daily temporal resolution of passive microwave brightness temperatures provides the most widely utilized observations to detect melt onset but are limited to a spatial resolution of 25 km. Wide-swath synthetic aperture radar (SAR) imagery provides a much higher spatial resolution (20–100 m) but melt onset detection remains challenging because of i) insufficient temporal resolution to facilitate accurate melt onset detection, ii) inconsistent viewing geometries and iii) limited image availability across the Arctic. Here, we construct high temporal resolution composite gamma nought backscatter products (1 day, 1–2 day and 2–4 day) using Sentinel-1 and RADARSAT-2 over a close-to-seamless revisit region located in northern Canadian Arctic and Greenland for estimating melt onset over Arctic sea ice in 2016 and 2017. We employ the necessary radiometric terrain flattening and local resolution weighting techniques to generate normalised backscatter over the entire study region, removing restrictions limiting analysis to a single sensor or track's swath width by integrating both ascending and descending passes into the composite products. Results indicate that higher temporal resolution multi-sensor composite gamma nought products (1 day) that make use of the most imagery provide a robust temporal evolution of the backscatter. This allows for more representative estimates of melt onset as it is easier to separate the melt onset threshold from winter variability that is otherwise a considerable challenge for SAR based melt onset algorithms because of inconsistent temporal resolution. Multi-sensor composite gamma naught melt onset detection is in good agreement with melt onset estimates derived from the Advance Scatterometer (ASCAT) backscatter values and passive microwave brightness temperatures over homogenous sea ice regions but very noticeable improvement was found within narrow channels and regions with more heterogeneous sea ice. In anticipation of the availability of data from even more SAR satellites with the launch of the RADARSAT Constellation Mission, the multi-sensor composite gamma nought approach presented here may offer the most robust approach to estimate the timing of melt onset over sea ice across the Arctic using high spatiotemporal resolution SAR.

1. Introduction

Recent surface air temperature (SAT) increases in the Arctic have been attributed to anthropogenic influence (Fyfe et al., 2013). Advection of warm and humid air over the Arctic sea ice resulting in downwelling longwave radiation increases is the dominant process that initializes melt onset (Mortin et al., 2016). Information on the timing of melt onset over sea ice is therefore important for understanding the response of the Arctic climate system to anthropogenic influence. An earlier melt onset facilitates the absorption of more solar radiation into the sea ice, leading to larger decreases in sea ice extent during the melt season (Perovich et al., 2007). Melt onset over Arctic sea ice has shifted to an earlier timing at a rate of −5.69 days per decade over the entire period from 1979 to 2017 (Bliss and Anderson, 2018) which is associated with decreasing trends in the Arctic's sea ice extent (Comiso, 2012; Stroeve et al., 2012).

Time series microwave remote sensing can be utilized for estimating the timing of melt onset over the Arctic sea ice because changes in microwave emission and scattering are reflective of the physical melt onset process. The most widely utilized techniques are those based on

* Corresponding author.
E-mail address: Stephen.howell@Canada.ca (S.E.L. Howell).

https://doi.org/10.1016/j.rse.2019.04.031
Received 10 December 2018; Received in revised form 26 April 2019; Accepted 27 April 2019
Available online 08 May 2019

high temporal resolution (1 day) passive microwave brightness temperatures time series values that use change thresholds to identify the transition from dry winter sea ice conditions to melt onset (e.g. Drobot and Anderson, 2001; Belchansky et al., 2004; Markus et al., 2009; Bliss and Anderson, 2014). Passive microwave brightness temperatures also allow for long term estimates of melt onset (1979 to present) but only at a spatial resolution of 25 km. There are also several techniques that use high temporal resolution (1–2 day) scatterometer backscatter observations which provide a higher spatial resolution (~2–5 km) but they are only available over a shorter time period (2000 to present) (e.g. Howell et al., 2006; Wang et al., 2011; Mortin et al., 2012; Mortin et al., 2014). C-band synthetic aperture radar (SAR) imagery provides the highest wide swath spatial resolution (20–100 m) and techniques have been developed to detect melt onset of Arctic sea ice (e.g. Livingstone et al., 1987; Onstott et al., 1987; Winebrenner et al., 1994; Kwok et al., 2003; Yackel et al., 2007; Mahmud et al., 2016) but it still remains challenging because of i) insufficient temporal resolution to facilitate accurate melt onset detection, ii) inconsistent viewing geometries and iii) limited image availability across the Arctic domain. Mahmud et al. (2016) successfully utilized RADARSAT-1 and RADARSAT-2 for melt onset detection in the northern Canadian Arctic Archipelago but noted that the temporal resolution of the imagery was a limitation with respect to representative spatiotemporal melt onset estimates.

With the recent launch of the European Space Agency's (ESA) Sentinel-1A (2014; S1A) and Sentinel-1B (2016; S1B) the potential for high resolution pan-Arctic melt onset detection from C-band SAR has increased. However, despite the considerable spatial coverage provided by S1A and S1B, there are still gaps across the Arctic and construction of high temporal resolution time series SAR datasets (i.e. 1–2 day) is still problematic. The upcoming launch of the RADARSAT Constellation Mission adds yet more C-band SAR sensors to the existing satellite image pool. Combining the RADARSAT Constellation Mission with S1A and S1B provides a unique opportunity to construct high temporal resolution datasets across the Arctic, analogous to what is possible from passive microwave brightness temperatures but at very high spatial resolution. In anticipation of the multiple C-band SAR satellites from S1A, S1B and the RADARSAT Constellation Mission, we suggest that a multi-sensor backscatter approach may offer the most robust approach to estimate the timing melt onset over Arctic sea ice from C-band SAR. In this analysis, we construct composite normalised gamma naught (γ_C^o; Small, 2011; Small, 2012) backscatter products at high temporal resolution from S1A, S1B and RADARSAT-2 SAR imagery and evaluate their utility for melt onset detection over Arctic sea ice.

2. Study area

The study area for this analysis is located in the northern Canadian Arctic and Greenland during the years of 2016 and 2017 (Fig. 1). This is a close-to-seamless revisit region imaged by S1A, S1B and RADARSAT-2 that contained a considerable number of overlapping images in 2016 and even more in 2017 (Fig. 2). Sea ice within the study region for 2016 and 2017 contains both landfast seasonal first-year ice (FYI) and multi-year ice (MYI) as well as the mobile MYI found in Arctic Ocean. The narrow channels and mix of ice types make it an ideal region to illustrate the benefits of high spatial resolution SAR for melt onset detection. Time series sample locations for FYI and MYI types were identified in both years to represent the aforementioned conditions and are indicated in Fig. 1.

3. Data

The primary datasets used in this analysis were C-band (wavelength, $\lambda = 5.5$ cm) SAR imagery from S1A and S1B Extra Wide (EW), S1A and S1B Interferometric Wide (IW) and RADARSAT-2 ScanSAR Wide (SCWA) acquired at dual polarization (HH + HV) from March to August over the northern Canadian Arctic Archipelago and Greenland (Fig. 1) in 2016 and 2017 (Table 1). The S1A and S1B imagery is freely available at the Copernicus Open Access Hub (https://scihub.copernicus.eu/dhus/#/home) and RADARSAT-2 imagery is available online for a fee at Natural Resources Canada's Earth Observation Data Management System (https://www.eodms-sgdot.nrcan-rncan.gc.ca).

To evaluate the representativeness of the γ_C^o products for 2016 and 2017, we used additional data from: i) the Advanced Scatterometer (ASCAT) single polarization (VV) Scatterometer Image Reconstruction (SIR; Early and Long, 2001) 4.45 km spatial resolution dataset available online from Brigham Young University at http://www.scp.byu.edu/data/Ascat/SIR/Ascat_sir.html; daily SAT from the extended Advanced Very High Resolution Radiometer (AVHRR) Polar Pathfinder dataset (APP-x; Key et al., 2014) available online from the NOAA National Centers for Environmental Information at https://www.ncdc.noaa.gov/cdr/atmospheric/extended-avhrr-polar-pathfinder-app-x; weekly in situ snow thickness values over FYI at Eureka, Nunavut (Fig. 1, red box) available online from the Canadian Ice Service (http://www.ec.gc.ca/glaces-ice/, see Archive followed by Ice Thickness Data); and finally 25 km spatial resolution estimates of the first date of melt onset from the Passive Microwave algorithm (PMW; Markus et al., 2009) available online from the NASA Cryosphere Science Research Portal at https://neptune.gsfc.nasa.gov/csb/ (see Data).

4. Construction of normalised composite gamma naught (γ_C^o) backscatter products

The ratio between the scattered and transmitted power of microwave energy is referred to as radar backscatter and the backscatter coefficient is this ratio expressed over a reference ground area (Ulaby et al., 1986). Depending on which reference area chosen, the scattering coefficient is different. Complete details with respect to scattering coefficient differences are provided in Small (2011) but briefly, the most common scattering coefficient is sigma naught (σ°) and is the result when the reference area is the ground area projected on an ellipsoid. Beta naught (β°) which is also referred to as radar brightness (see also Raney et al., 1994) is the simplest definition, least encumbered by an Earth model, placing the reference area is in the sensor's slant range plane, with no requirement for an ellipsoidal or terrain Earth model. Finally, gamma naught (γ°) is the result when the reference area is in the plane perpendicular to the local look direction, representing the local area that the radar system actually sees.

Terrain-induced radiometric distortions are present in SAR backscatter maps unless they are properly compensated. Knowledge of modern radar satellite state vectors and timing annotations has improved to the point where tie-point free geolocation of each point in a radar image is now routinely possible at better than 1 m accuracy. Accuracies achieved with multiple radar sensors were reported in Schubert et al. (2012) and sub-meter accuracy for the two Sentinel-1 satellites was reported in Schubert et al. (2017). Use of high quality SAR sensor geometric calibration enables routine automatic connection of each SAR pixel with a corresponding digital elevation model (DEM) location on the Earth's surface. Correction of the *position* of each measurement is called geocoding, and is a standard step available in many software packages, whereby the applicable Doppler (azimuth) and range equations are solved. Although the geometry was corrected in the geocoding step, unless further steps are taken, the effect of terrain on the local radar brightness (*radiometry*) will remain tied to a simple ellipsoidal Earth model and not the local terrain and the variable resolution within a single acquisition will also remain (Small, 2011).

The approach we use to generate the multi-sensor γ_C^o image products accounts for the aforementioned problems and is universal in that it is applicable to both marine and terrestrial regions across the SAR image. Although the focus of this study is Arctic sea ice, for which terrain correction using a DEM is not possible but it is still required to obtain the local ellipsoidal height, a complete description of the approach is provided because terrain correction is only one component of

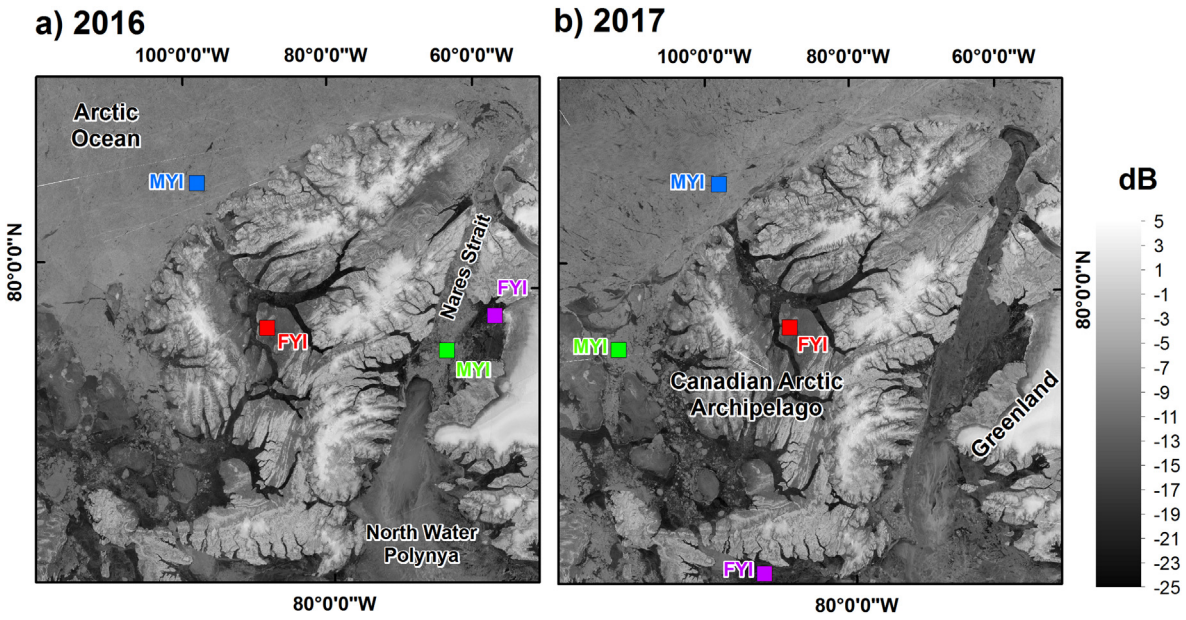

Fig. 1. Multi-sensor γ_C^o backscatter (dB) map of study region on (a) March 19, 2016 using data from Sentinel-1A and RADARSAT-2 and on (b) March 24, 2017 using data from Sentinel-1A, Sentinel-1B and RADARSAT-2. The first-year ice (FYI) and multi-year ice (MYI) sample sites locations color code corresponds to the time series plots in Figs. 6, 10, 12 and 13. (a) and (b) contain modified Copernicus Sentinel data (2017). RADARSAT-2 Data and Products © MacDonald, Dettwiler and Associates Ltd. (2016; 2017) - All Rights Reserved. RADARSAT is an official trademark of the Canadian Space Agency. (For interpretation of the references to color in this figure, the reader is referred to the web version of this article.)

the overall processing chain illustrated in Fig. 3. The S1A, S1B and RADARSAT-2 images are first converted to beta naught (β°). Then, following Small (2011), radiometric terrain distortions are modeled by summing up all DEM-facet contributions to each SAR image pixel. DEM locations blocked from observation by radar shadow are accounted for in the image simulation by not including such DEM-facets in the sum. Once the map of local contributing area is complete, the original β° image is normalised using that map. This newly normalised backscatter is initially in radar geometry but can then be easily geocoded in a further step to produce a radiometrically terrain corrected (RTC; γ_T^o) backscatter image in map geometry.

These RTC images are properly normalised radiometrically for terrain distortions, but the variable resolution within a single acquisition can remain quite considerable. To lower the noise and ensure that the image and backscatter properties become even more uniform, a second stage of processing is used that combines data from multiple tracks into a single wide-area backscatter composite image. A set of N_i available RTC images acquired within a time window i are combined by applying their local resolution (i.e. the reciprocal of the local illuminated area used to normalise them) as a weighting function. The methodology behind this step is discussed in detail by Small (2012) which results in a single backscatter composite per defined time window i (e.g. 1 day, 1–2 day and 2–4 day). An example of these final multi-sourced γ_C^o products for 1 day time window using 16 and 20 SAR images is shown in Figs. 4 and 5, respectively. These final multi-sourced γ_C^o products have a spatial resolution of 400 m with relatively spatially homogenous image properties with lower noise than a single acquisition, making them a useful "analysis ready data" level 3 product for higher level application studies. They have for example been previously applied to normalising terrain distortions to successfully map forest-type using seasonal backscatter signatures over the whole of the Alps (Rüetschi et al., 2018). This is the first known application to a relatively flat landscape. The DEM utilized in this study (Santoro and Strozzi, 2012; https://doi.org/10.1594/PANGAEA.779748) was deemed to be

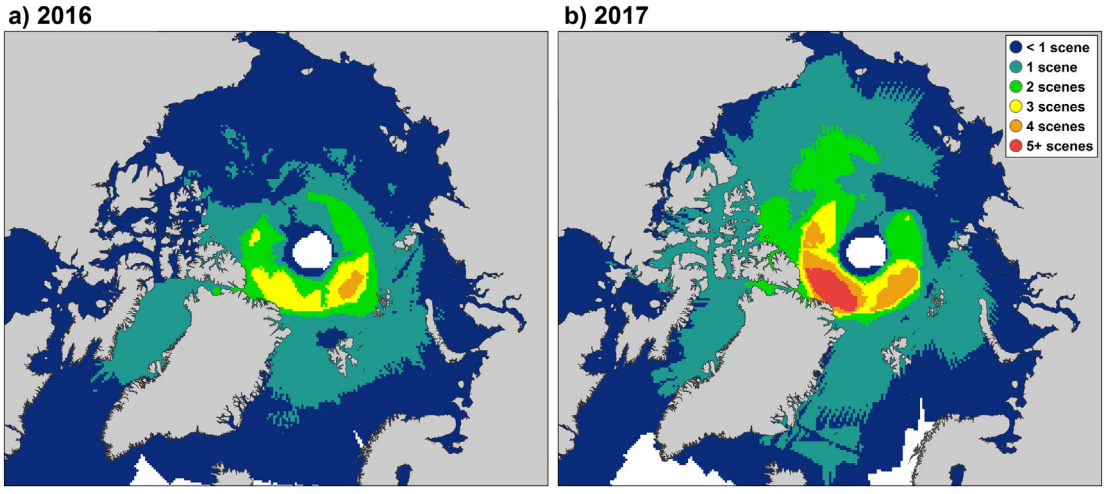

Fig. 2. Spatial distribution of available imagery (scenes per day) from Sentinel-1A, Sentinel-1B and RADARSAT-2 for (a) April 2016 and (b) April 2017.

Table 1
SAR image products and counts used in this analysis for 2016 and 2017.

Image product	Spatial resolution (m)	Incident angle	Swath (km)	Count 2016	Count 2017
RADARSAT-2 SCWA-SGF	100	20.0°-49.3°	500	280	321
Sentinel-1 EW-GRDM	90	18.0°-47.0°	400	1699	2428
Sentinel-1 IW-GRDH	20	31.0°-46.0°	250	301	681

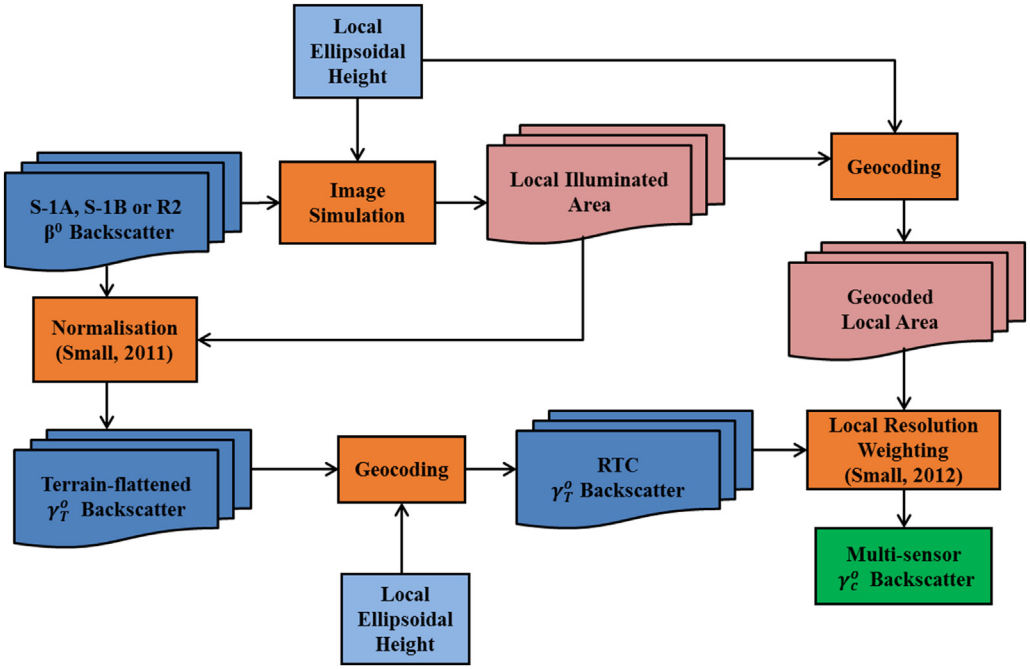

Fig. 3. Processing chain for construction of the composite γ_C^o backscatter products.

sufficient for product generation at 400 m spatial resolution, but given sufficient DEM resolution and quality, achieving 100 m spatial resolution or higher would only be a matter of computational and storage resources. Finally, it should be noted that although, this processing chain was applied to both HH and HV polarizations, the higher noise floor associated with the HV channel resulted in numerous temporal gaps in the γ_C^o time series and therefore, we restricted this analysis to only the γ_C^o products at HH polarization.

5. Temporal evolution of γ_C^o products from winter to melt onset

Remotely sensed techniques using time series sigma nought (σ°) values have a long history for detecting melt onset over Arctic sea ice (e.g. Livingstone et al., 1987; Onstott et al., 1987; Winebrenner et al., 1994; Yackel et al., 2001; Kwok et al., 2003; Mortin et al., 2014; Mahmud et al., 2016). To our knowledge, γ° or γ_C^o has not been previously utilized for time series melt onset detection over Arctic sea ice. Moreover, γ° is less sensitive to incidence angle effects (Small, 2011) making it potentially more robust than σ° for melt onset detection.

5.1. First-year ice (FYI)

Over the FYI sample site in 2016 and 2017, γ_C^o backscatter values for all constructed SAR products were relatively low during the pre-melt winter period from day of year (DOY) 90–150 because the near snow-ice interface is cold resulting in low basal layer snow brine volume, a relatively small dielectric permittivity and low volume scattering (Fig. 6). Surface scattering largely controls C-band backscatter at these cold temperatures. The variability in the winter backscatter time series is known to be influenced by atmospheric forcing as a function of snow thickness causing changes in brine volumes in the snow and at the snow-sea ice interface that are reflected in the backscatter coefficient (Barber et al., 1995; Barber and Nghiem, 1999). Changing incidence angles also contribute to backscatter variability over FYI during the winter (Mäkynen and Karvonen, 2017; Mahmud et al., 2018). The higher γ_C^o values in 2016 versus 2017 are likely the result of a rougher sea ice surface surrounding the sample site in 2016, as evident from Fig. 7, and not atmospheric forcing. Moreover, the rougher surface in 2016 was also associated with thicker snow on sea ice (Fig. 8) which would likely buffer against the influence of atmospheric forcing on the γ_C^o backscatter.

The major difficulty with using a threshold backscatter change for melt onset detection over FYI from SAR is separating winter backscatter variability from the first major upturn in backscatter that denotes melt onset, especially when temporal gaps are present in the time series. Warming first causes an increase in the brine volume at the snow-sea ice interface, increasing volume scattering that facilitates the major backscatter upturn (Drinkwater, 1989; Barber et al., 1995). For the sample site in 2016, the melt onset upturn was indeed difficult to pinpoint (~DOY170) because of high γ_C^o variability during the winter, combined with some temporal gaps in the time series for all products (Fig. 6a). In 2017, the upturn in γ_C^o was also difficult to identify using the 2–4 day R2 product given the presence of temporal gaps however, the γ_C^o upturn was clearly apparent after DOY160 for the 1-day S1AB + R2 and 1–2 day S1AB products (Fig. 6b).

To explore the utility of these products beyond surface roughness conditions surrounding the local time series scale at Eureka, we calculated the April (DOY90–120) mean γ_C^o of all FYI landfast pixels (~500,000) in the study region for all constructed SAR products in both years. For each product, FYI pixels were identified using the Kwok (2004) threshold as having a γ_C^o value less than −14.5 dB. The variability in mean April γ_C^o for all products, for both years is illustrated by

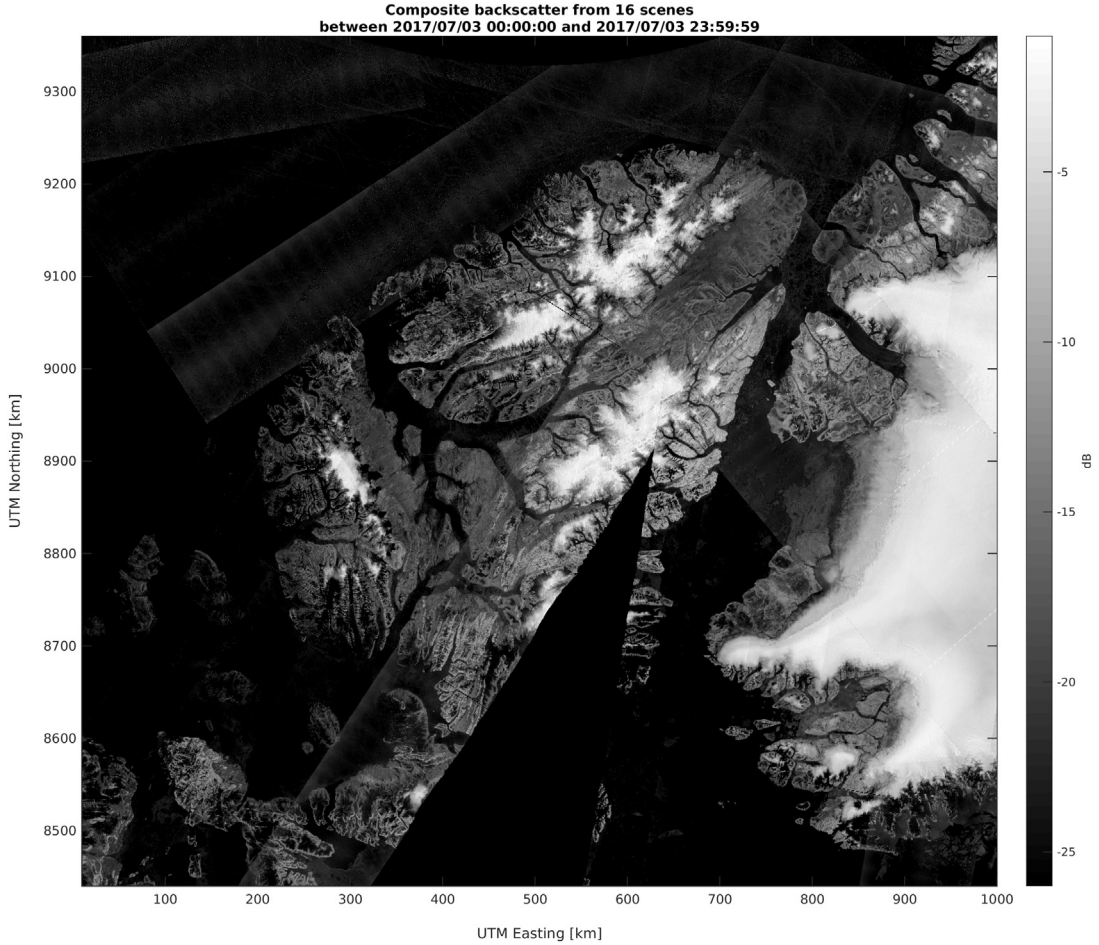

Fig. 4. Multi-sensor γ_C^o backscatter (dB) for (a) July 3, 2017 using 16 images from Sentinel-1A and Sentinel-1B. Contain modified Copernicus Sentinel data (2017).

boxplots in Fig. 9. In 2016, γ_C^o winter variability was similar for all products and suggests additional imagery in the multi-sensor product does not appreciably impact its winter variability (Fig. 9a). However, higher temporal resolution multi-sourced 1–2 day S1A + R2 product certainly provided a γ_C^o temporal evolution with less temporal gaps compared to the 2–4 day products (Fig. 6a). There was more imagery utilized for the γ_C^o products in 2017 compared to 2016 (Table 1) and winter γ_C^o variability was subsequently lower in 2017 (Fig. 9). Moreover, the largest amount of imagery was utilized for the 1–2 day S1AB and 1 day S1AB + R2 products in 2017 that in turn experienced the lowest winter γ_C^o variability (Fig. 9b).

Image availability from SAR typically results in a trade-off between image homogeneity and temporal blurring using local resolution weighting (Small, 2012) but with the considerable amount of imagery available over the study region in 2017, it is evident that both image homogeneity and temporal resolution can be maintained. Specifically, Figs. 6b and 9b illustrate that the mean weighted backscatter for the higher temporal resolution SAR products that take into account all available imagery (i.e. increased number of looks) contributes to less variable γ_C^o values and in turn a more robust temporal evolution of γ_C^o over FYI during the winter period. This suggests that for multi-sourced γ_C^o products with higher temporal resolution and more included imagery, separating the melt onset upturn from winter γ_C^o variability over FYI is less problematic.

5.2. Multi-year ice (MYI)

Over the MYI sample site in 2016 and 2017, γ_C^o for all products was high and stable during the pre-melt winter period (DOY90–150) (Fig. 10) because air bubbles cause volume scattering to occur within the ice. Over MYI which is brine free, the first major downturn in backscatter is identified as melt onset because ice volume scattering is masked by increases in liquid water content within the snowpack (Winebrenner et al., 1994). The differences in temporal evolution were close to negligible between the γ_C^o products, although more temporal gaps were apparent in 2016 than 2017 (Fig. 10). With the exception of the 2–4 day R2 product in 2017 that contained considerable temporal gaps, all the downturn in γ_C^o was easily distinguishable on DOY158 and DOY165 for 2016 and 2017, respectively in all products (Fig. 10). The winter stability of γ_C^o resulting from an absence of brine induced changes on γ_C^o allows identifying the melt onset downturn over MYI less problematic than FYI. Moreover, the winter backscatter over MYI is less sensitive to incidence angle variations (Mahmud et al., 2018).

Analogous to FYI, we also calculated the mean April (DOY90–120) γ_C^o of all MYI landfast pixels (~250,000) in the study region for all constructed SAR products. MYI pixels were identified using the Kwok (2004) threshold as having a γ_C^o value greater than −14.5 dB. Boxplots of the mean April γ_C^o over landfast MYI during the winter for all constructed SAR products are shown in Fig. 11 and confirm that γ_C^o variability is less than over FYI. Fig. 11 also indicates that the mean weighted backscatter for the highest temporal resolution multi-sensor SAR products (i.e. 1–2 day S1AB and 1 day S1AB + R2) has less of an impact on γ_C^o winter variability over MYI compared to FYI since it is already quite stable (i.e. absence of brine). Despite this, the highest temporal resolution SAR products that utilized the most imagery certainly facilitated an improved and more robust γ_C^o temporal evolution over MYI compared to lower temporal resolution product (Fig. 10).

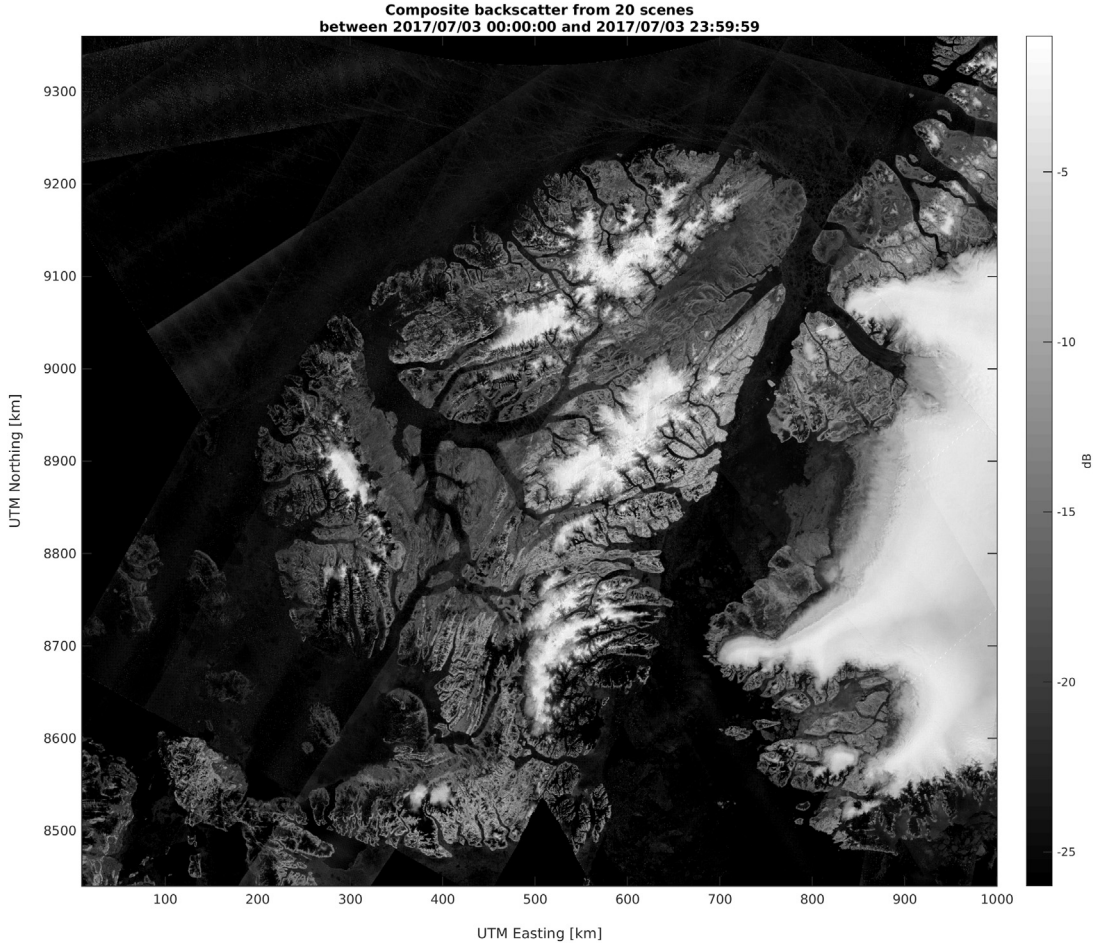

Fig. 5. Multi-sensor γ_C^o backscatter for July 3, 2017 using 20 images from Sentinel-1A, Sentinel-1B, and RADARSAT-2. Contains modified Copernicus Sentinel data (2017). RADARSAT-2 Data and Products © MacDonald, Dettwiler and Associates Ltd. (2017) - All Rights Reserved. RADARSAT is an official trademark of the Canadian Space Agency.

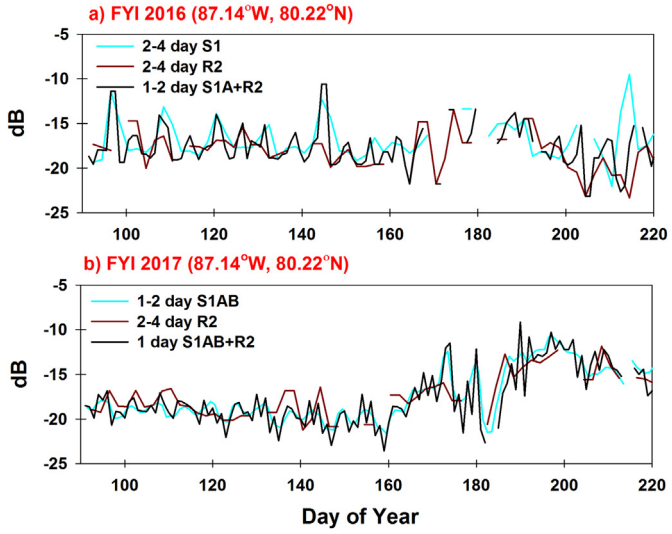

Fig. 6. Time series of γ_C^o backscatter (dB) products over seasonal first-year ice (FYI) for (a) 2016 and (b) 2017.

5.3. Comparison with ASCAT σ°, passive microwave estimates of melt onset and surface air temperature

The high temporal resolution of satellite-based passive microwave brightness temperatures and scatterometer backscatter has contributed to these sensors being widely utilized for melt onset detection, with the trade-off being moderate to coarse spatial resolution. Considering that the multi-sensor γ_C^o S1A + R2 product in 2016 and S1AB + R2 product in 2017 provided the highest achievable temporal resolution in our study region, we now compare these products to ASCAT σ°, melt onset from the PMW algorithm and SAT.

At the sample sites for 2016 and 2017, variability from the multi-sensor γ_C^o products was larger than ASCAT σ° at the daily time scale, but the overall temporal evolution was remarkably similar (Figs. 12, 13). Correlations (r) between ASCAT σ° and multi-sensor γ_C^o ranged from $r = 0.81–0.93$. The multi-sensor γ_C^o also correlated reasonably well with SAT ranging between $r = 0.48–0.71$ denoting changes in dielectrics are responding to changes in SAT that are in turn reflected inγ_C^o. The strength of relationship is similar to Yackel et al. (2001) who found SAT explained between 30 and 55% of the variation in the backscatter.

For all test sites, the first major upturn (FYI) or downturn (MYI) of the multi-sensor γ_C^o generally corresponded with SAT approaching or rising slightly above 0 °C (Figs. 12, 13). This correspondence has been widely reported by previous studies identifying factors that are associated with melt onset detected by microwave remote sensing (e.g. Yackel et al., 2001; Belchansky et al., 2004; Mortin et al., 2014; Mahmud et al., 2016). For the first date of melt onset from the PMW algorithm, only the landfast MYI site in 2016 (Fig. 12b) and the mobile MYI site in 2017 (Fig. 13a) were in good agreement with the multi-sensor γ_C^o melt onset transition. The PMW algorithm detected melt

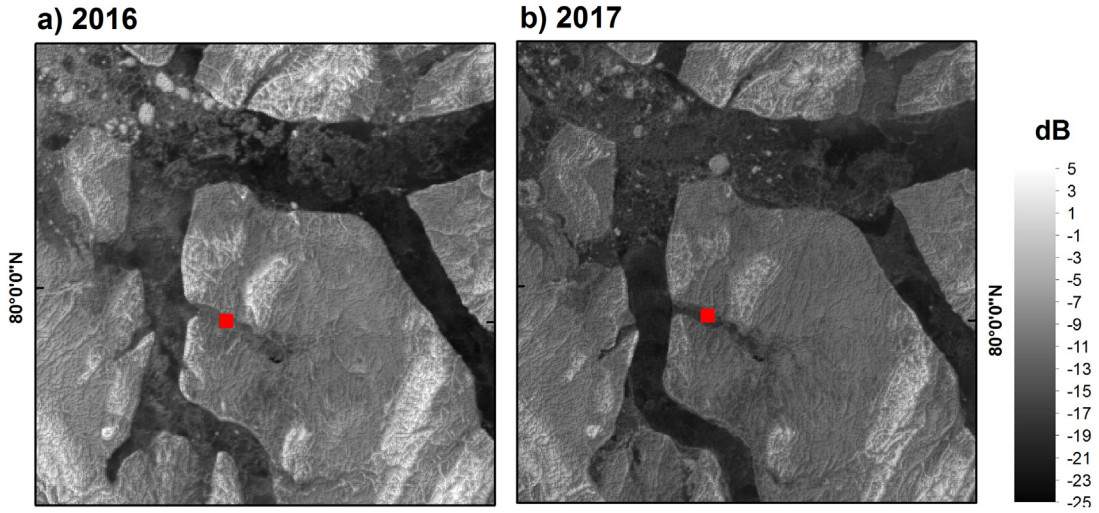

Fig. 7. Multi-sourced γ_C^o backscatter (dB) image on (a) March 19, 2016 and (b) March 24, 2017. The red square corresponds to the location of the snow depth on sea ice measurements and the seasonal first-year ice (FYI) γ_C^o time series shown in Fig. 6. (a) and (b) contain modified Copernicus Sentinel data (2017). RADARSAT-2 Data and Products © MacDonald, Dettwiler and Associates Ltd. (2016; 2017) - All Rights Reserved. RADARSAT is an official trademark of the Canadian Space Agency. (For interpretation of the references to color in this figure legend, the reader is referred to the web version of this article.)

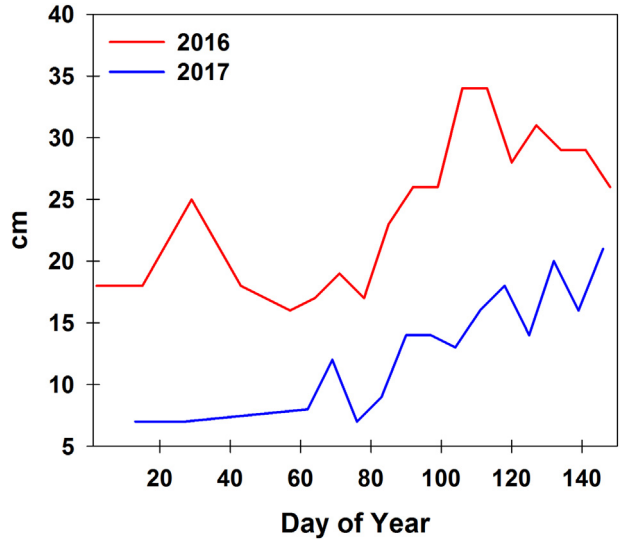

Fig. 8. Time series of snow depth on sea ice (cm) at Eureka, Nunavut for 2016 and 2017.

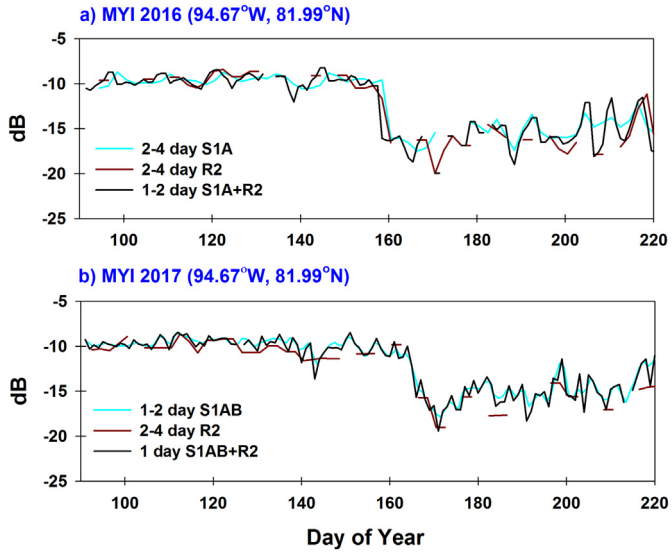

Fig. 10. Time series of γ_C^o backscatter (dB) products over seasonal multi-year ice (MYI) for (a) 2016 and (b) 2017.

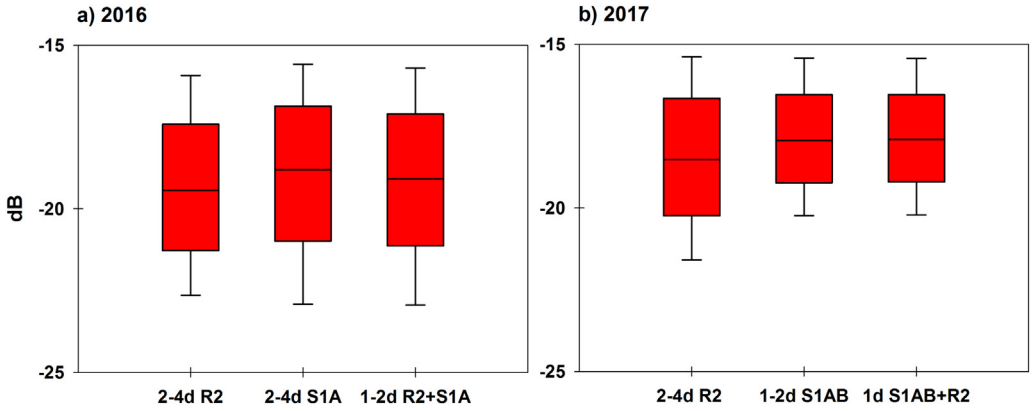

Fig. 9. Boxplots of the mean γ_C^o backscatter (dB) for each constructed product (x-axis) calculated over landfast first-year ice (FYI) during the winter period from day of year 90–120 for (a) 2016 and (b) 2017.

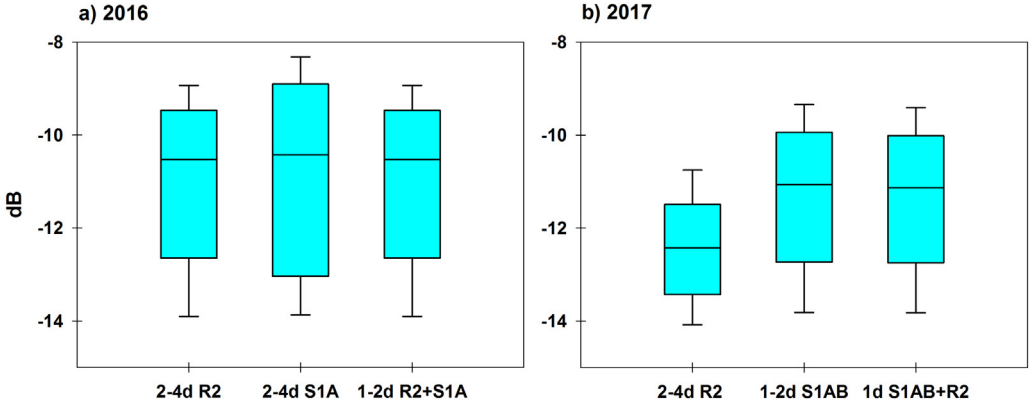

Fig. 11. Boxplots of the mean γ_C^o backscatter (dB) values for each constructed product (x-axis) calculated over landfast multi-year ice (MYI) during the winter period from day of year 90–120 for (a) 2016 and (b) 2017.

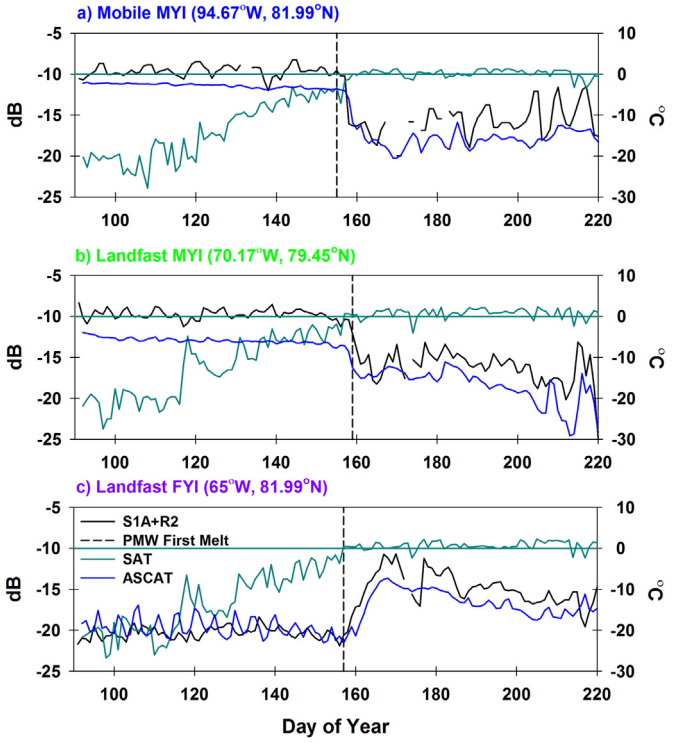

Fig. 12. Time series of γ_C^o backscatter (dB), the ASCAT sigma naught (σ°) backscatter, surface air temperature (SAT) and the first date of melt onset detected by the passive microwave (PMW) algorithm in 2016 over (a) mobile multi-year ice (MYI), (b) landfast MYI and (c) landfast seasonal first-year ice (FYI).

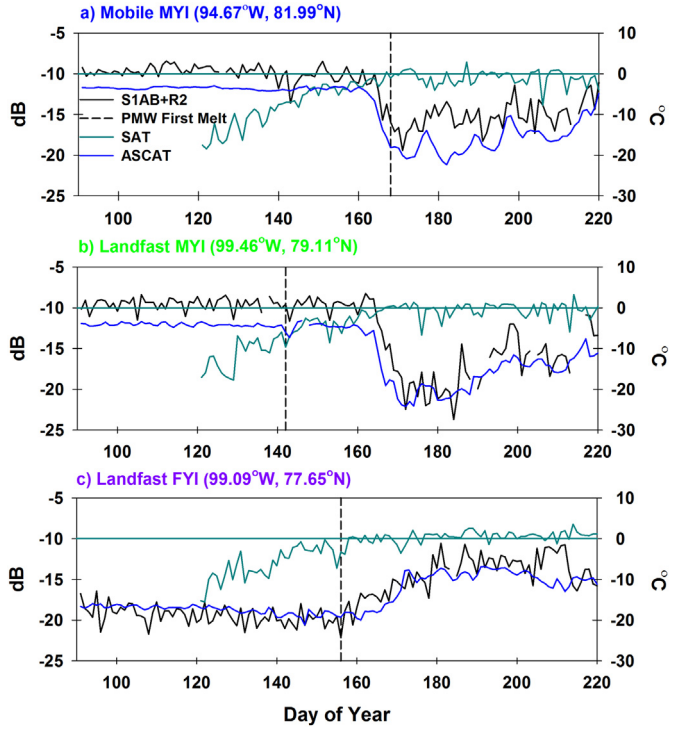

Fig. 13. Time series of γ_C^o backscatter (dB), the ASCAT sigma naught (σ°) backscatter, surface air temperature (SAT) and the first date of melt onset detected by the passive microwave (PMW) algorithm in 2017 over (a) mobile multi-year ice (MYI), (b) landfast MYI and (c) landfast seasonal first-year ice (FYI).

onset too early for the remaining samples sites (Figs. 12a, c, 13b, c). Very early melt detection was apparent at the 2017 landfast MYI test site when both ASCAT and multi-sensor γ_C^o showed that the first major downturn was much later (Fig. 13b). Possible explanations for the early PMW algorithm melt detection as well as a spatial inter-comparison are presented in the following section. Overall, with temporal evolution of the multi-sensor γ_C^o being similar to ASCAT σ°, the melt onset transitions were relatively easy to detect, which is a considerable improvement compared to previous studies using time series SAR for melt detection (e.g. Yackel et al., 2007; Mahmud et al., 2016) where the datasets suffered from irregular temporal resolution inconsistency.

6. Spatially mapping multi-sensor γ_C^o detected melt onset

6.1. Melt onset transition retrieval

We now make use of γ_C^o at its highest available temporal resolution (S1A + R2 product in 2016 and S1AB + R2 in 2017) to develop a melt onset threshold retrieval approach for spatial application and evaluation. Given that such a multi-sensor γ_C^o time series has never been utilized for melt onset detection over sea ice, a different strategy with different thresholds was required compared to previous algorithms based on σ° values. Our intent in this study is to provide a simple, yet robust approach for comparison purposes, as the focus of this paper is not melt onset algorithm development. Accordingly, we also develop an approach to map melt onset in our study region from ASCAT σ° to best compare against multi-sensor γ_C^o. We acknowledge that application of

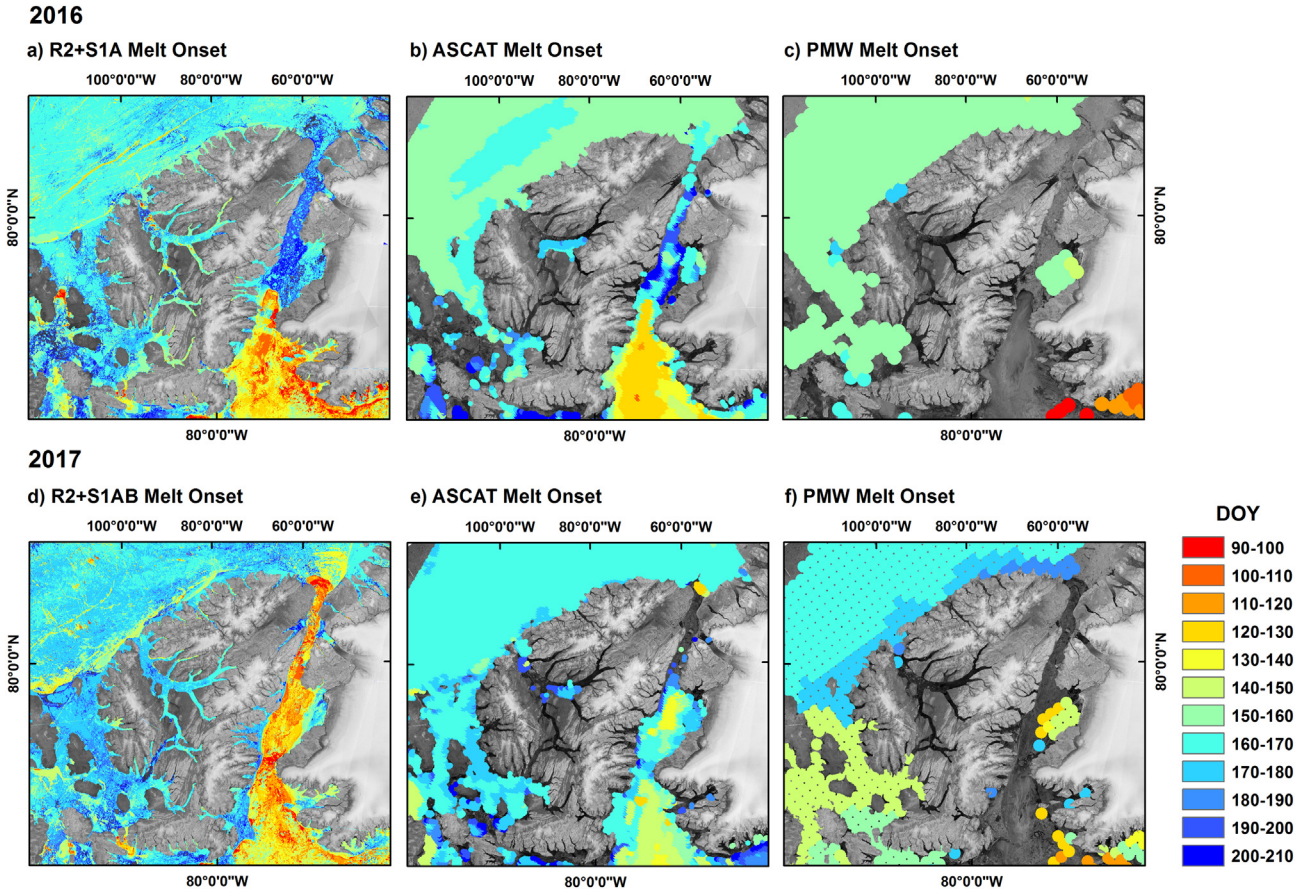

Fig. 14. Melt onset spatial distribution as detected by multi-sensor γ_C^o (a and d), ASCAT sigma naught (σ°) (b and e) and the passive microwave (PMW) algorithm (e and f) for 2016 and 2017. (a-f) contain modified Copernicus Sentinel data (2016–2017). RADARSAT-2 Data and Products © MacDonald, Dettwiler and Associates Ltd. (2016; 2017) - All Rights Reserved. RADARSAT is an official trademark of the Canadian Space Agency.

these algorithms beyond this study region may require modifications.

For multi-sensor γ_C^o melt onset detection, we first calculate the winter mean γ_C^o during April for each pixel. We use the winter mean γ_C^o as a baseline from which to flag melt onset for a pixel if γ_C^o departs at a certain absolute value threshold from it. Next, we separate FYI and MYI using a value of −14.5 dB (Kwok, 2004) because the magnitude of the γ_C^o upturn (FYI) is different than the magnitude of the γ_C^o downturn (MYI) as shown in both Figs. 12 and 13. In order to determine a melt onset γ_C^o absolute value threshold, we iterated through numerous values in 0.25 dB increments starting with at 3 dB for each ice type, arriving at 8 dB for MYI and 5 dB for FYI. The 5 dB threshold for FYI was sufficient to avoid most early melt onset detection from time series winter γ_C^o variability and still capture the first major upturn (not shown). When the 5 dB threshold was also applied to MYI, melt onset detection was too early, especially over mobile MYI in the presence of leads (not shown). Using the 8 dB threshold for MYI best reduced early melt onset detection in these mobile MYI regions however, this threshold was too aggressive over FYI as it resulted in very late melt onset (not shown). Overall, in this study region, using the aforementioned thresholds for FYI and MYI best ensured the γ_C^o detected melt onset fell within the first significant upturn or downturn of the γ_C^o time series and was representative of each ice type.

For ASCAT, we also calculated the winter mean backscatter during April for each pixel and used it as a baseline from which to flag melt onset. However, unlike γ_C^o, there was no improvement in using separate thresholds for FYI and MYI (not shown) and as a result, we selected a threshold of 5 dB to denote melt onset with ASCAT σ° in our study region. Based on the time series plots in Figs. 12 and 13, the 5 dB threshold was sufficient to avoid early melt onset detection from winter variability while at the same time not being overly aggressive to result in very late melt onset as would be the case with higher threshold values over MYI. Divergent sea ice motion resulting in leads was not an appreciable problem for early melt onset detection with ASCAT because unless there is a sustainable amount of open water, ice will still be the dominant scattering mechanism given ASCAT's moderate spatial resolution.

6.2. Spatial distribution of melt onset

Fig. 14 illustrates melt onset timing spatially for the multi-sensor γ_C^o, ASCAT σ° and the PMW algorithm for 2016 and 2017. It is important to note that the 2017 melt onset map is more representative because it was based on a 1 day γ_C^o time series with fewer spatio-temporal gaps than 2016. The most striking feature in Fig. 14 is the level of spatial detail captured by the multi-sensor γ_C^o products in both years. Early melt onset was expected within the surrounding region of North Water Polynya and south of the ice arch in Nares Strait. Early melt onset was also expected in the south west region of the study area as it is known to be a location for recurring polynyas (Smith and Rigby, 1981). Coarse PMW algorithm retrievals were unable to detect melt onset in Nares Strait and the narrow channels located in the Canadian Arctic Archipelago. ASCAT performed slightly better in the aforementioned regions but spatial gaps were still apparent.

While the multi-sensor γ_C^o certainly provides unprecedented spatial detail, leads caused by divergent sea ice motion are better resolved. As a result, in both 2016 and 2017 the multi-sensor γ_C^o algorithm detected these leads as earlier melt onset within the Arctic Ocean MYI pack as well as along the shear zone between the Arctic Ocean and northern

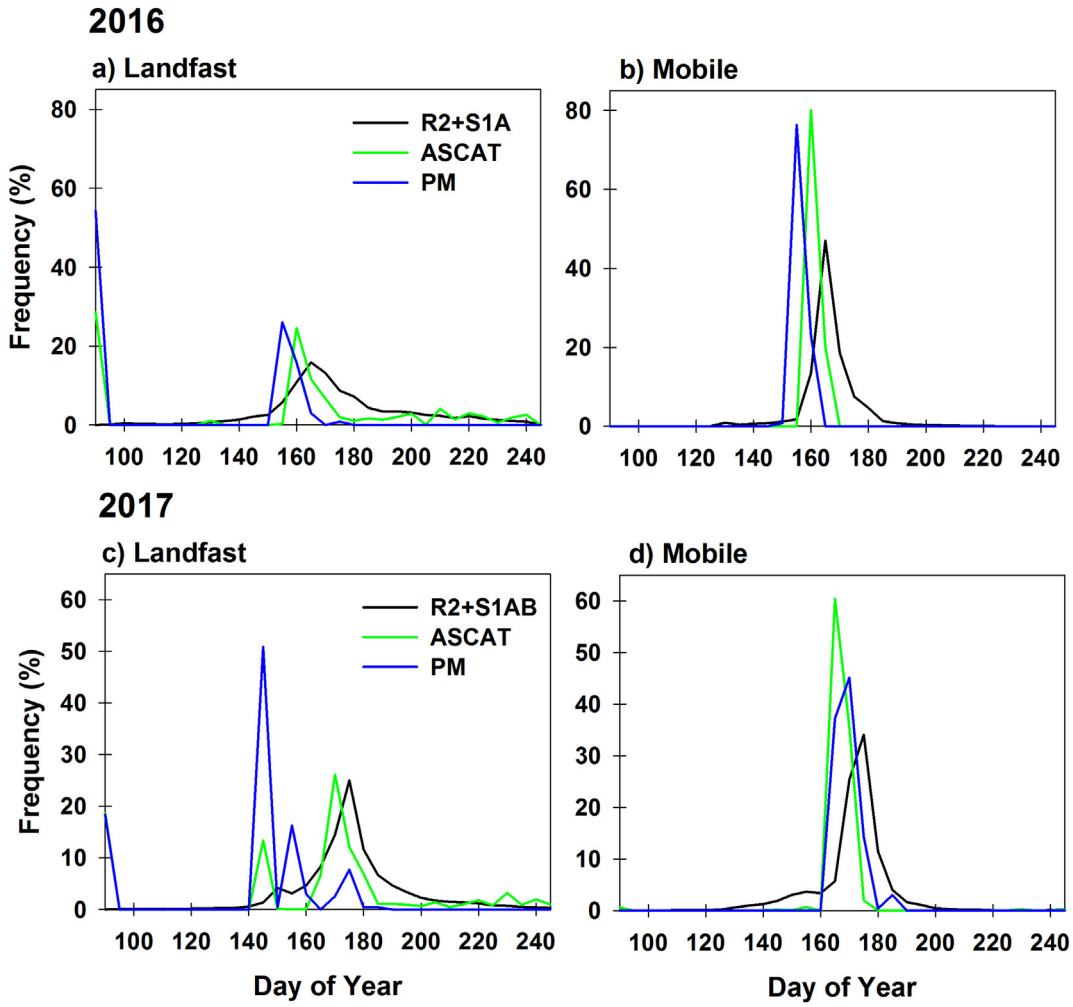

Fig. 15. Frequency distribution (%) of melt onset date (day of year) estimated from multi-sensor γ_C^o, ASCAT sigma naught (σ°) the passive microwave (PMW) algorithm for landfast ice (a and c) and mobile ice in the Arctic Ocean (b and d).

Canadian Arctic Archipelago (Fig. 14a, d). These dynamic sea ice features are less of a concern for the lower resolution ASCAT and PMW satellite sensors as the open water does not exert sufficient influence on their larger pixels to be classified as melt onset (Fig. 14b, c, e, f).

The highest frequency range of multi-sensor γ_C^o melt onset detection was observed between DOY155–165 in 2016 and between DOY145–175 in 2017 (Fig. 15). For both 2016 and 2017, these date ranges were in good agreement with the spatial distribution of SAT between −5 °C and 5 °C (Fig. 16) when melt onset is expected to be detected from microwave sensors (Barber et al., 1995; Yackel et al., 2007). Melt onset was detected first by the PMW algorithm, ASCAT and then multi-sensor γ_C^o (Table 2; Fig. 15). The standard deviation was high for the multi-sensor γ_C^o approach (Table 2) as a result of leads on the Arctic Ocean MYI pack, but more so from early melt detection in Nares Strait and the North Water Polynya (Fig. 14a, d).

The multi-sensor γ_C^o approach likely detects slightly later melt onset dates than ASCAT because MYI regions are better isolated in the multi-sensor γ_C^o product. When MYI is 'sampled' in the ASCAT pixel it almost always captures some FYI since MYI floes are found at sub-resolution of 4.45 km ASCAT. Therefore, the brine effect with FYI that contributes to earlier melt onset detection is likely picked up in MYI samples for ASCAT. The PMW algorithm likely detects melt onset earlier than ASCAT and multi-sensor γ_C^o because the shorter wavelengths used in the PMW algorithm are more sensitive to changes in liquid water content at the surface. It has been shown that small increases in liquid water will cause the scattering to be dominated by water instead of dry snow (Linlor, 1980; Hallikainen et al., 1986). The process is enhanced within FYI compared to MYI because of the strong influence of temperature on brine volume and dielectric permittivity and in turn the backscatter (Barber and Thomas, 1998). This is particularly apparent in our study for 2017 as the PMW algorithm detected the majority of very early melt onset over heterogeneous MYI and FYI landfast regions on DOY145 whereas ASCAT and multi-sensor γ_C^o did not (Figs. 14d–f, 15c). This very early melt detected by the PMW algorithm on DOY145 for 2017 was coincident with SAT in the range of −5 °C to 0 °C which is sufficient to be detected at lower PMW frequencies (Fig. 16d). One of our temporal evolution time series sample sites was within this region and confirmed that SAT increases circa DOY145 were indeed sufficient to detect melt onset using the PMW (Fig. 13b). The SAT increases circa DOY145 did contribute to change in the backscatter of both the multi-sensor γ_C^o and ASCAT σ° values but not of sufficient magnitude to detect melt onset (Fig. 13b).

7. Conclusions

In this analysis, we employed radiometric terrain flattening and local resolution weighting techniques described by Small (2011) and Small (2012) to construct high temporal resolution γ_C^o products (1 day, 1–2 day and 2–4 day) from S1A, S1B and RADARSAT-2 SAR imagery. We then evaluated the γ_C^o products for melt onset detection over Arctic sea ice as compared to ASCAT and the PMW algorithm in 2016 and 2017 for a study region located in the Canadian Arctic and Greenland.

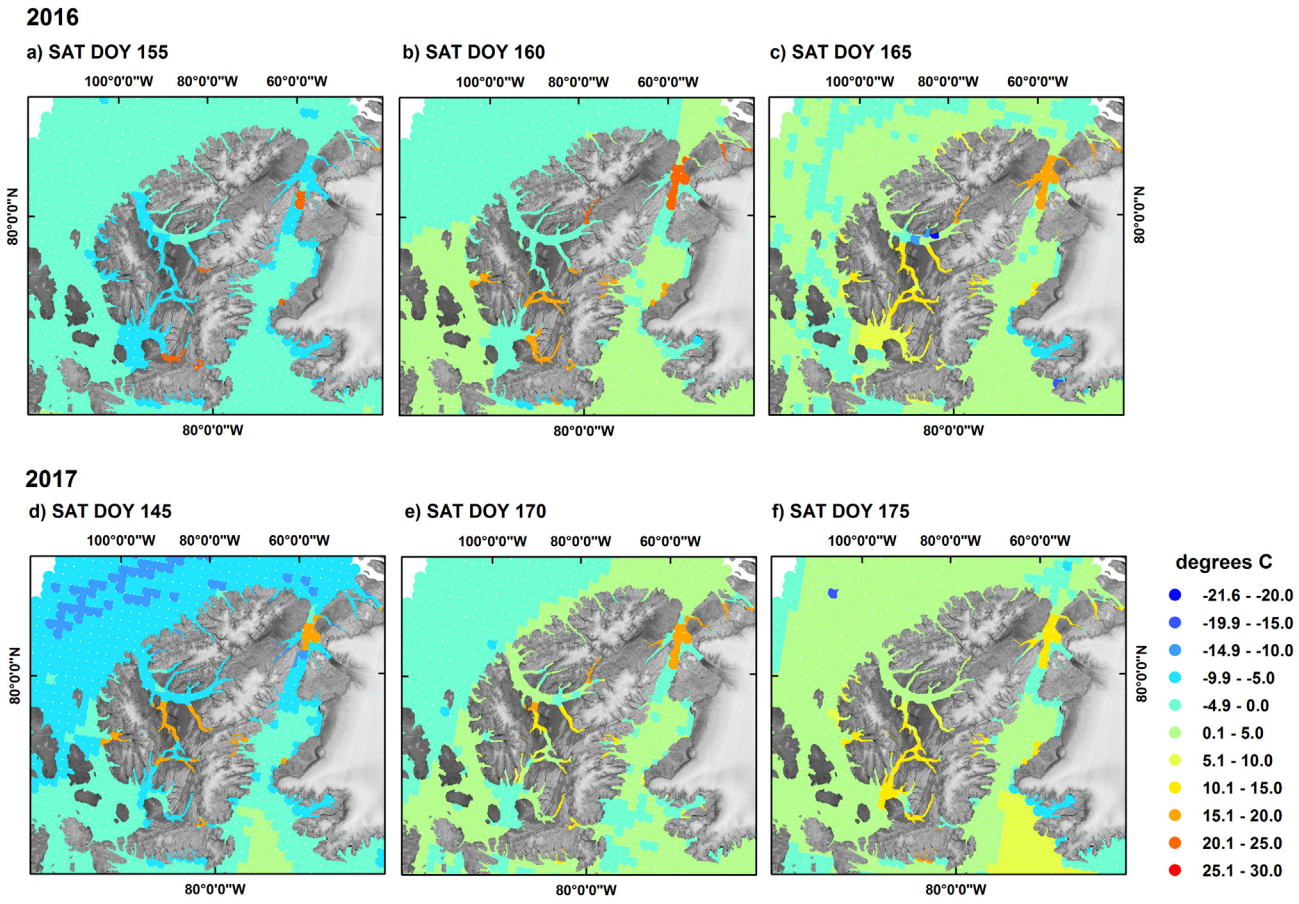

Fig. 16. Surface air temperature (SAT) spatial distribution in the study region on day of year (DOY) (a) 155, (b) 160 and (c) 165 for 2016 and DOY (d) 155, (e) 170 and (f) 175 for 2017.

Table 2
Mean melt onset timing dates for each sensor with standard deviation in brackets.

Approach	2017	2016
Multi-sensor γ_C^o	167 (44.2)	168 (43.9)
ASCAT σ°	166 (17.7)	161 (20.5)
PMW algorithm	155 (14.8)	152 (14.28)

The weighted γ_C^o mean for the higher temporal resolution multi-sourced SAR products that take into account the most imagery facilitates more homogenous (less variable) γ_C^o values and enhances the temporal stability of γ_C^o. This was particularly apparent with the 2017 multi-sensor γ_C^o product that used more imagery than the 2016 multi-sensor γ_C^o. The temporal evolution from the multi-sensor γ_C^o was found to be consistent with temporal evolution of ASCAT σ°. This was found to be particularly useful over FYI and provided improved separability between dry winter conditions and melt onset which have been a significant challenge for SAR-based melt onset algorithms. Estimating melt onset over sea ice the study region using highest temporal resolution the multi-sensor γ_C^o products in both years resulted in an unprecedented level of detail with respect to the spatial distribution of melt onset in both years. Melt onset was found to be coincident in its spatial distribution with SAT approaching 0 °C associated with earlier melt in 2016 and later melt in 2017. Multi-sensor γ_C^o melt onset detection was also found to be in good agreement with ASCAT and the PMW algorithm over homogenous sea ice regions but very noticeable improvement was found within narrow channels and regions with more heterogeneous sea ice. However, the high spatial resolution from multi-sensor γ_C^o products detected erroneous melt onset in leads within the Arctic Ocean MYI pack as well as along the shear zone between the Arctic Ocean and northern Canadian Arctic Archipelago. Localised sea ice dynamics will therefore need to be taken into consideration for future melt onset algorithm development from multi-sensor γ_C^o SAR products. However, the ability of the multi-sensor γ_C^o SAR products to identify leads suggests these products could be utilized for lead detection studies.

Given that the timing of melt onset influences the end of summer sea ice extent in the Arctic (Perovich et al., 2007) and that positive trends in downwelling longwave radiation are linked to positive melt onset trends across the Arctic (Mortin et al., 2016), continuing to provide melt onset estimates is important for understanding the response of sea ice to a warming Arctic. Indeed, the PMW algorithm provides the best long-term measure of melt onset but SAR imagery can provide more robust estimates, especially as the spatiotemporal constraints of its application are dwindling with the current generation of C-band SAR satellites (i.e. S1A, S1B and RADARSAT-2). Efforts to implement retrieved sea ice geophysical variables from SAR in data assimilation systems are currently underway and eventually SAR imagery will find utility in seasonal forecasting systems (e.g. Komarov and Buehner, 2017). In this study, we have shown excellent potential for the use of multi-sensor backscatter from SAR to provide high quality melt onset information over Arctic sea ice which would be of significant value to data assimilation systems. In anticipation of the availability of data from even more SAR satellites with the launch of the RADARSAT Constellation Mission, the multi-sensor γ_C^o approach presented here may offer the most robust approach to estimate the timing of melt onset over sea ice across the Arctic.

Acknowledgments

The authors wish to thank the Polar Space Task Group who coordinated the SAR acquisitions that made this work possible.

References

Barber, D.G., Nghiem, S.V., 1999. The role of snow on the thermal dependence of microwave backscatter over sea ice. J. Geophys. Res. 104 (C11), 25789. https://doi.org/10.1029/1999JC900181.

Barber, D.G., Thomas, A., 1998. The influence of cloud cover on the radiation budget, physical properties and microwave scattering coefficient of first-year and multi-year sea ice. IEEE Trans. Geosci. Remote Sens. 361, 38–50. https://doi.org/10.1109/36.655316.

Barber, D.G., Papakyriakou, T.N., LeDrew, E.F., Shokr, M.E., 1995. An examination of the relation between the spring period evolution of the scattering coefficient and radiative fluxes over landfast sea ice. Int. J. Remote Sens. 16 (17), 3343–3363.

Belchansky, G.I., Douglas, D.C., Mordvintsev, I.N., Platonov, N.G., 2004. Estimating the time of melt onset and freeze onset over Arctic sea-ice area using active and passive microwave data. Remote Sens. Environ. 92, 21–39.

Bliss, A.C., Anderson, M.R., 2014. Snowmelt onset over Arctic sea ice from passive microwave satellite data: 1979–2012. Cryosphere 8, 2089–2100. https://doi.org/10.5194/tc-8-2089-2014.

Bliss, A.C., Anderson, M.R., 2018. Arctic sea ice melt onset timing from passive microwave-based and surface air temperature-based methods. J. Geophys. Res. Atmos. 123, 9063–9080. https://doi.org/10.1029/2018JD028676.

Comiso, J.C., 2012. Large decadal decline of the Arctic multiyear ice cover. J. Clim. 25, 1176–1193. https://doi.org/10.1175/JCLI-D-11–00113.1.

Drinkwater, M., 1989. LIMEX'87 ice surface characteristics: implications for C-band SAR backscatter signatures. IEEE Trans. Geosci. Remote Sens. 27 (5), 501–513. https://doi.org/10.1109/TGRS.1989.35933.

Drobot, S.D., Anderson, M.R., 2001. An improved method for determining snowmelt onset dates over Arctic sea ice using Scanning Multichannel Microwave Radiometer and Special Sensor Microwave/Imager data. J. Geophys. Res. 106, 24033–24049. https://doi.org/10.1029/2000JD000171.

Early, D.S., Long, D.G., 2001. Image reconstruction and enhanced resolution imaging from irregular samples. IEEE Trans. Geosci. Remote Sens. 39 (2), 291–302. https://doi.org/10.1109/36.905237.

Fyfe, J.C., von Salzen, K., Gillett, N.P., Aurora, V.K., Flato, G.F., McConnell, J.R., 2013. One hundred years of Arctic surface temperature variation due to anthropogenic influence. Sci. Rep. 3 (1), 2645. https://doi.org/10.1038/srep02645.

Hallikainen, M.T., Ulaby, F.T., Abdelraz, M., 1986. Dielectric properties of snow in the 3 to 37 GHz range. IEEE Trans. Antennas Propag. 34 (11), 1329–1340.

Howell, S.E.L., Tivy, A., Yackel, J.J., Scharien, R.K., 2006. Application of a SeaWinds/QuikSCAT sea ice melt algorithm for assessing melt dynamics in the Canadian Arctic Archipelago. J. Geophys. Res. 111 (C7), C07025. https://doi.org/10.1029/2005JC003193.

Key, J., Wang, W., Yinghui, L., NOAA CDR Program, 2014. NOAA Climate Data Record of AVHRR Polar Pathfinder Extended (APP-X), Version 1. NOAA National Centers for Environmental Informationhttps://doi.org/10.7289/V5MK69W6. (May 2018).

Komarov, A.S., Buehner, M., 2017. Automated detection of ice and open water from dual-polarization RADARSAT-2 images for data assimilation. IEEE Trans. Geosci. Remote Sens. 55 (10), 5755–5769. https://doi.org/10.1109/TGRS.2017.2713987.

Kwok, R., 2004. Annual cycles of multiyear sea ice coverage of the Arctic Ocean: 1999–2003. J. Geophys. Res. 109 (C11), C11004. https://doi.org/10.1029/2003JC002238.

Kwok, R., Cunningham, G.F., Nghiem, S.V., 2003. A study of the onset of melt over the Arctic Ocean in RADARSAT synthetic aperture radar data. J. Geophys. Res. 108 (C11), 3363. https://doi.org/10.1029/2002JC001363.

Linlor, W.L., 1980. Permittivity and attenuation of wet snow between 4 and 12 GHz. J. Appl. Phys. 51 (5), 2811–2816. https://doi.org/10.1063/1.327947.

Livingstone, C.E., Singh, K.P., P, K., Gray, A.L., 1987. Seasonal and regional variations of active/passive microwave signatures of sea ice. IEEE Trans. Geosci. Remote Sens. 25 (2), 159–173. https://doi.org/10.1109/TGRS.1987.289815.

Mahmud, M.S., Howell, S.E.L., Geldsetzer, T., Yackel, J., 2016. Detection of melt onset over the northern Canadian Arctic Archipelago sea ice from RADARSAT, 1997–2014. Remote Sens. Environ. 178, 59–69. 56(11), 6686–6698. https://doi.org/10.1016/j.rse.2016.03.003.

Mahmud, M., Geldsetzer, T., Howell, S.E.L., Yackel, J.J., Nandan, V., Scharien, R.K., 2018. Incidence angle dependence of HH-polarized C- and L-band wintertime backscatter over Arctic sea ice. IEEE Trans. Geosci. Remote Sens. https://doi.org/10.1109/TGRS.2018.2841343.

Mäkynen, M., Karvonen, J., 2017. Incidence angle dependence of first-year sea ice backscattering coefficient in Sentinel-1 SAR imagery over the Kara Sea. IEEE Trans. Geosci. Remote Sens. 55 (11), 6170–6181. https://doi.org/10.1109/TGRS.2017.2721981.

Markus, T., Stroeve, J.C., Miller, J., 2009. Recent changes in Arctic sea ice melt onset, freezeup, and melt season length. J. Geophys. Res. 114, C12024. https://doi.org/10.1029/2009JC005436.

Mortin, J., Schrøder, T.M., Hansen, A.W., Holt, B., McDonald, K.C., 2012. Mapping of seasonal freeze–thaw transitions across the pan-Arctic land and sea ice domains with satellite radar. J. Geophys. Res. 117 (C8), C08004. https://doi.org/10.1029/2012JC008001.

Mortin, J., Howell, S.E.L., Wang, L., Derksen, C., Svensson, G., Graversen, R.G., Schrøder, T.M., 2014. Extending the QuikSCAT record of seasonal melt–freeze transitions over Arctic sea ice using ASCAT. Remote Sens. Environ. 141, 214–230. https://doi.org/10.1016/j.rse.2013.11.004.

Mortin, J., Svensson, G., Graversen, R.G., Kapsch, M.-L., Stroeve, J.C., Boisvert, L.N., 2016. Melt onset over Arctic sea ice controlled by atmospheric moisture transport. Geophys. Res. Lett. 43, 6636–6642. https://doi.org/10.1002/2016GL069330.

Onstott, R.G., Grenfell, T.C., Mätzler, C., Luther, C.A., Svendsen, E.A., 1987. Evolution of microwave sea ice signatures during early summer and midsummer in the marginal ice zone. J. Geophys. Res. 92 (C7), 6825–6835. https://doi.org/10.1029/JC092iC07p06825.

Perovich, D.K., Nghiem, S.V., Markus, T., Schweiger, A., 2007. Seasonal evolution and interannual variability of the local solar energy absorbed by the Arctic sea ice–ocean system. J. Geophys. Res. Oceans 112 (C03005). https://doi.org/10.1029/2006JC003558.

Raney, R.K., Freeman, A., Hawkins, R., Bamler, R., 1994. A plea for radar brightness. In: International Geoscience and Remote Sensing Symposium (IGARSS). 2. pp. 1090–1092.

Rüetschi, M., Schaepman, M., Small, D., 2018. Using multitemporal Sentinel-1 C-band backscatter to monitor phenology and classify deciduous and coniferous forests in Northern Switzerland. Remote Sens. 10 (55). https://doi.org/10.3390/RS10010055.

Santoro, M., Strozzi, T., 2012. Circumpolar digital elevation models > 55° N with links to geotiff images. PANGAEA. https://doi.org/10.1594/PANGAEA.779748.

Schubert, A., Small, D., Jehle, M., Meier, E., 2012. COSMO-SkyMed, TerraSAR-X, and RADARSAT-2 geolocation accuracy after compensation for earth-system effects. In: IEEE International Geoscience and Remote Sensing Symposium IGARSS, Munich, Germany, pp. 3301–3304. https://doi.org/10.1109/IGARSS.2012.6350598.

Schubert, A., Miranda, N., Geudtner, D., Small, D., 2017. Sentinel-1A/B combined product geolocation accuracy. Remote Sens. 9, 607. https://doi.org/10.3390/rs9060607.

Small, D., 2011. Flattening gamma: radiometric terrain correction for SAR imagery. IEEE Trans. Geosci. Remote Sens. 49 (8), 3081–3093. https://doi.org/10.1109/TGRS.2011.2120616.

Small, D., 2012. SAR backscatter multitemporal compositing via local resolution weighting. In: IEEE International Geoscience and Remote Sensing Symposium IGARSS, Munich, Germany, pp. 4521–4524. https://doi.org/10.1109/IGARSS.2012.6350465.

Smith, M., Rigby, B., 1981. Distribution of Polynyas in the Canadian Arctic, Polynyas in the Canadian Arctic, Occasional Paper 45. Canadian Wildlife Service, Environment Canada, pp. 7–28.

Stroeve, J.C., Serreze, M.C., Holland, M.M., Kay, J.E., Maslanik, J., Barrett, A.P., 2012. The Arctic's rapidly shrinking sea ice cover: a research synthesis. Clim. Chang. 110 (3–4), 1005–1027. https://doi.org/10.1007/s10584-011-0101-1.

Ulaby, F.T., Moore, R.E., Fung, A.K., 1986. Microwave Remote Sensing: Active and Passive. vols. 1, 2 and 3 Addison-Wesley Publishing Company, MA.

Wang, L., Wolken, G.J., Sharp, M.J., Howell, S.E.L., Derksen, C., Brown, R.D., Markus, T., Cole, J., 2011. Integrated pan-Arctic melt onset detection from satellite active and passive microwave measurements, 2000–2009. J. Geophys. Res. 116 (D22103). https://doi.org/10.1029/2011JD016256.

Winebrenner, D.P., Nelson, E.D., Colony, R., West, R.D., 1994. Observation of melt onset on multiyear Arctic sea ice using ERS 1 synthetic aperture radar. J. Geophys. Res. 99 (C11), 22425–22441. https://doi.org/10.1029/94JC01268.

Yackel, J.J., Barber, D.G., Papakyriakou, T.N., 2001. On the estimation of spring melt in the north water polynya using RADARSAT-1. Atmosphere-Ocean 39, 195–208.

Yackel, J.J., Barber, D.G., Papakyriakou, T.N., Breneman, C., 2007. First-year sea ice spring melt transitions in the Canadian Arctic Archipelago from time-series synthetic aperture radar data, 1992–2002. Hydrol. Process. 21 (2), 253–265.